J. Fluid Mech. (2001), *vol.* 447, *pp.* 377–408.
DOI 10.1017/S0022112001005870 Printed in the United Kingdom

On the miscible Rayleigh–Taylor instability: two and three dimensions

By Y.-N. YOUNG[1], H. TUFO[2], A. DUBEY[1] AND R. ROSNER[1]

[1]Department of Astronomy and Astrophysics, University of Chicago, Chicago, IL 60637, USA

[2]Department of Computer Science, University of Chicago, IL 60637, USA

(Received 15 December 1999 and in revised form 5 December 2000)

We investigate the miscible Rayleigh–Taylor (RT) instability in both two and three dimensions using direct numerical simulations, where the working fluid is assumed incompressible under the Boussinesq approximation. We first consider the case of randomly perturbed interfaces. With a variety of diagnostics, we develop a physical picture for the detailed temporal development of the mixed layer: we identify three distinct evolutionary phases in this development, which can be related to detailed variations in the growth of the mixing zone. Our analysis provides an explanation for the observed differences between two- and three-dimensional RT instability; the analysis also leads us to concentrate on the RT models which (i) work equally well for both laminar and turbulent flows, and (ii) do not depend on turbulent scaling within the mixing layer between fluids. These candidate RT models are based on point sources within bubbles (or plumes) and their interaction with each other (or the background flow). With this motivation, we examine the evolution of single plumes, and relate our numerical results (for single plumes) to a simple analytical model for plume evolution.

1. Introduction

The phenomenology of mixing due to the Rayleigh–Taylor (RT) instability, the instability of an interface separating fluids of different densities subject to gravity (Chandrasekhar 1961 and references therein), can be summarized as follows. Bubbles (spikes) of lighter (heavier) fluid penetrate into the heavier (lighter) fluid, and leave behind them a region of mixed fluid. As the instability enters the nonlinear regime, fluid motions in this mixing region become highly irregular. The envelope, or edge, of the mixing region is observed to be defined by fast large-scale motion, which tends to be dominated by the merging of expanding smaller bubbles (spikes). The irregular fluid motions within the mixing zone are often regarded as 'turbulent' in the sense that the flow is chaotic in the wake of the bubbles (spikes).

A principal focus of experimental and theoretical study has been the general properties of this mixing zone, whose broadening in time is commonly characterized by the 'envelope velocity' (V_e) and the penetration lengths h_b and h_s (for bubbles and spikes, respectively). Using simple analytical models for the interpenetration of the two fluids, one can show (Youngs 1984 and references therein) that in the nonlinear regime V_e is proportional to time (t), and that the penetration depths $h_{b,s}$ are proportional to t^2 and depend linearly on the gravitational acceleration g and the Atwood number A ($\equiv (\rho_1 - \rho_2)/(\rho_1 + \rho_2)$, where $\rho_{1,2}$ is the density of the heavier (lighter) fluid, respectively), i.e.

$$h_{b,s} = \alpha_{b,s} g A t^2. \tag{1.1}$$

α can be thought of as a measure of the efficiency of potential energy release; experimental measurements of α give results in the range $0.03 \sim 0.06$ (see Sharp 1984; Read 1984 and Youngs 1984). Most recently, Schneider, Dimonte & Remington (1998) show that α lies in the range 0.05–0.06 for an Atwood number of 0.34; as the Reynolds number is high ($\sim 10^5$) in these linear electric motor (LEM) experiments, the instability enters the nonlinear regime within several e-folding times (~ 0.9 ms), so that the above scaling law seems to hold from the time that the first few measurements of mixing zone width are made.

There are many possible reasons for the observed variation of α found in the literature, when scaling of the form (1.1) is observed during the experiment or simulation. Setting aside problems such as incompletely controlled experiments or insufficiently resolved computations, it is important to establish whether the nonlinear (long-time) evolution of the instability is sensitive to details in the experiment such as initial conditions; and to what extent one can really talk about universal scaling of the mixed layer width. These questions have been addressed to some extent in the literature. For example, Youngs (1991) has studied the variation of α with time during the course of RT evolution; he reported that larger values of $\alpha \sim 0.06$ occur during the early phase of the three-dimensional problem, before any development of small-scale turbulence; however, as small-scale motions develop, Youngs (1991) reports that the three-dimensional growth rate slows to that characteristic of the two-dimensional case ($\alpha \sim 0.04$). It is also found that α may depend on the Atwood number A as $A \rightarrow 1$ (G. Dimonte, private communication). In a variation on this theme, it has been observed in simulations that α can depend on dimensionality: α for three-dimensional calculations is found to be larger than for two-dimensional simulations. Sakagami & Nishihara (1990) have found α for three-dimensional calculations to be at least 4 times higher than for two-dimensional simulations (in spherical systems); and more detailed phenomena can be found in Yabe, Hoshino & Tsuchiya (1991), Li (1993) and He *et al.* (1999). Town & Bell (1991) found larger values for α in three-dimensional only during the early nonlinear stage, and showed that as small-scale three-dimensional turbulence developed, the three-dimensional growth slows to that of the two-dimensional case, similar to results reported by Youngs (1991). Other three-dimensional numerical simulations, including investigations of single-mode initial perturbation (Dahlburg & Gardner 1990; Tryggvason & Unverdi 1990; Kane & Arnett 1998) and more general initial perturbations (Cook & Dimotakis 2001), obtain a range of values for α generally restricted to $0.05 \sim 0.06$. In this paper we also explore the dependence of the RT instability on dimensionality. We focus on quantitative comparisons between two and three dimensions, and these comparisons provide more complete insights into the understanding of RT instability. In the case of experiments conducted with gases, it has also been shown that the interface perturbation growth can be measurably affected by mass diffusion effects between the two layers (Duff, Harlow & Hirt 1962). These experimental and computational results argue strongly that the precise value of α is sensitive to a variety of details in the experiments, ranging from the specific nature of the initial state to the dimensionality of the perturbation. It is the aim of this paper to initiate a study of this issue: we consider some of the effects which influence the value of the scaling coefficient α as the Rayleigh–Taylor instability develops in time; a central question we address is whether a single scaling regime is always to be expected during the course of nonlinear Rayleigh–Taylor development.

In order to make our study more tractable, we have focused only on the low Atwood number regime. The advantage of this regime is that numerical techniques developed for incompressible flows can be readily applied to flows satisfying the Boussinesq

equations; such computations are substantially more economical than calculations of the fully compressible problem, and thus allow a more extensive exploration of the parameter space other than Atwood number. Physically, our calculations correspond to, for example, cases in which the density contrast is introduced by the distribution of a scalar field (e.g. salt or temperature), for which the Atwood number is usually small because the density varies weakly with the scalar 'concentration'. Species or temperature diffusion occurs in such systems, and so is included in our simulations; we are therefore considering the miscible version of the Rayleigh–Taylor instability. In this Boussinesq approximation, the Atwood number $A \to 0$ and yet gA is a finite constant. An essential element in computations in this regime is that the calculations remain fully resolved throughout the evolution of the instability. This important constraint limits the range of allowable Prandtl number Pr (ratio of viscosity to thermal diffusivity) or Schmidt number Sc (ratio of viscosity to species diffusivity) in our calculations; we typically take these ratios to be of order unity. Tryggvason (1988) and Aref & Tryggvasono (1989) have adopted similar ideas in their earlier studies of immiscible Rayleigh–Taylor instability; however, in their case, the density is not coupled to a scalar field, and the buoyancy term in the Boussinesq Navier–Stokes equations (induced by the sharp density gradient across the interface) is the only term related to the weak stratification.

There are unfortunately few experimental studies of this regime: Linden, Redondo & Youngs (1994) have studied the miscible Rayleigh–Taylor instability experimentally, and via simulations. In their experiments, they place a layer of brine above a layer of fresh water, separated by an aluminium barrier. The experiment is initiated by sliding the barrier horizontally through one sidewall; the Atwood numbers in their experiments are in the range of $10^{-3} \sim 10^{-2}$ (as the density contrast due to the brine concentration is small when compared to the ambient density) and the Schmidt number Sc is $\sim 10^3$. Their experimental estimates for α are around 0.044. Linden *et al.* (1994) also performed numerical simulations for an Atwood number $A = 0.2$, and (numerical) Schmidt number of order unity. After imposing various perturbations at the interface, and determining α as a function of the ratio of the initial displacement of the fluid to the perturbation wavelength, they concluded that the smaller this ratio is, the higher the value of α. These authors argued that the removal of the barrier in the experiment corresponds to a long-wavelength perturbation at the interface, and therefore the comparison between numerical simulation and experiments makes sense only if the long-wavelength perturbation is included as part of the initial perturbation in the simulation. By implication, they thus suggest that the value of α obtained even in the long-time limit can depend on the initial conditions; in other words, these systems have long-term memory that is not erased by turbulent motions within the mixing interface. The dependence of RT instability on the initial conditions has recently been studied by Cook & Dimotakis (2001). In this paper, we focus on a study of the physical effects which determine α, and in particular investigate effects which lead to a departure from simple t^2 scaling of the mixing zone depth. A detailed study of the scaling law itself is now in progress, and led by G. Dimonte (the α group).

Our paper is organized as follows. We first formulate the problem, outline the numerics, and present evidence for the convergence and accuracy of our calculations. In the following section (§ 3) we summarize our results for multi-mode interface perturbations. We next discuss existing (analytical) models relevant to our studies (§ 4), which motivate a synthesis of a new model; in the following section (§ 5) we explore these ideas in more detail via numerical studies of isolated plume evolution in both two and three dimensions. Our conclusions are presented in § 6.

2. Formulation and methods

2.1. *Formulation of the problem*

We consider two vertically stacked fluid layers of different density, governed by the Boussinesq equations in a rectangular box (Chandrasekhar 1961). We adopt periodic boundary conditions along the horizontal directions; the top and bottom boundaries are no flux and no slip. Under the Boussinesq approximation, density variations only appear in the buoyancy term, and are small when compared to the mean density. There are a variety of ways of achieving a small density jump across the horizontal interface: one may choose gases of slightly different mean molecular weight, or a single fluid into which a 'contaminant' is added (such as temperature, sugar or salt in water) which changes the fluid's density slightly. Such vertical density variation depends linearly on temperature: colder (heavier) fluid sinks and warmer (lighter) fluid floats as gravity points downwards. Thus, in our formulation, the density jump across the interface is replaced by (for example) a temperature difference: colder fluid on top of warmer fluid. The equations for the miscible, incompressible, Rayleigh–Taylor instability in the Boussinesq limit are then essentially the incompressible Navier–Stokes equations coupled to an advection–diffusion equation for the 'contaminant', here temperature:

$$\partial_t \boldsymbol{u} + (\boldsymbol{u}\cdot\nabla)\boldsymbol{u} = -\nabla P + \nu\nabla^2\boldsymbol{u} + \beta g\, T\hat{\boldsymbol{g}}, \tag{2.1}$$

$$\nabla\cdot\boldsymbol{u} = 0, \tag{2.2}$$

$$\partial_t T + (\boldsymbol{u}\cdot\nabla)T = \kappa\nabla^2 T \tag{2.3}$$

(ν is the kinematic viscosity, β is the volumetric expansion coefficient, and κ is the thermal diffusivity.) We remark that the initial, unperturbed temperature profile diffuses on the diffusion time scale. We further remark that one could alternatively treat the case of weak stratification via a vertically imposed salinity (or any other type of concentration) gradient; in this way, one is able to explore a wide range of Prandtl/Schmidt numbers. There can be a variety of top and bottom boundary conditions for the scalars, such as fixing values or fixing fluxes at the boundaries. In our simulations, we adopt no-flux boundary conditions, which are typical in a run-down experiment. It is important to note here that since our equations allow for temperature diffusion, they are equivalent to systems in which the 'contaminant' is salt and allow for saline diffusion, or to systems describing two miscible fluids of slightly different density and allow for mass diffusion.

In our simulations, we are interested only in regimes where the thermal diffusion time is much longer than the dynamical time scales of interest. The reason for this constraint is as follows. Unlike the case of immiscible Rayleigh–Taylor instability, the presence of thermal diffusion formally does not allow for a static background temperature profile prior to any perturbation. Nevertheless, as we perturb the temperature at the interface, we find that if the diffusivity is sufficiently small, then the initial growth of the perturbation is exponential and thus mimics the linear regime in standard stability analyses for which an initial static equilibrium exists. Thus, long thermal diffusion times are essential if the dynamics is to be dominated by the Rayleigh–Taylor instability. The same kind of argument applies in the saline case, or in the case where mass diffusion can occur. Thus, we do not expect to see diffusion effects as reported by Duff *et al.* (1962); and our results indeed show that at least in the linear regime, our growth rates are the same as in the inviscid non-diffusive case.

Our problem is defined by a number of distinct spatial and temporal scales: the perturbation wavelength(s) λ (for single-mode perturbation) or spatial perturbation spectrum (for multi-mode perturbation), the amplitude of the initial displacement of

the fluid at the interface a_λ, and the initial interface thickness d. Two time scales are of most interest here: the dynamical time defined by the free-fall time and the scalar diffusion time. In the present study, we focus on cases where the dynamical time scale is much smaller than the diffusion time scale. In this limit, the diffusive interface between the hot and cold material remains more or less fixed at width d throughout the evolution; the computation spatial resolution is then required to at least resolve this interface throughout the calculation. Furthermore, we impose perturbations of amplitude a such that $a \geqslant d$ in order to capture the initial perturbation properly. Finally, the range of Atwood numbers we explore is consistent with values obtained in laboratory experiments for the miscible RT instability; and the ratio of viscosity to diffusivity is kept to values greater than or equal to 1.

2.2. *Numerics: methods and validation*

We have used two distinct numerical codes to solve the above equations, based on our desire to ensure that our results are independent of the computational method used to solve equations (2.1)–(2.3). We have compared both the mixing zone extent and the evolution of fluid structures (obtained from these two codes), to determine the fidelity of our calculations: the two codes lead to results within the expected range of errors for the same initial conditions and boundary conditions.

The first code is based on the use of pseudospectral methods to simulate the RT instability. The spatial discretization is Fourier in the periodic, horizontal directions and Chebyshev in the gravitational direction. The temporal discretization is third-order Adams–Bashforth for the nonlinear terms and Crank–Nicholson for the Laplacian terms. We use Werne's tau-correction scheme to achieve incompressibility (Werne 1995); the code is parallelized using MPI (Dubey & Clune 1999), and has been run on the Cray-T3E supercomputer at PSC. The second code is based on the spectral-element method (Tufo & Fischer 2001). It combines the spectral accuracy/efficiency and the geometric flexibility of finite elements, and has been widely applied to a variety of problems.

Figure 1(*a*) demonstrates the satisfactory agreement between the two codes. We plot the penetration depth h of the single-mode perturbation as a function of time τ. The solid line is from a spectral-element code, and the dashed line is from a spectral code. The spectral resolution is 256 by 512 and the spectral-element code has an equival number of total grid points for this comparison. The average difference in h is as small as 10^{-4}. By comparing results between spectral-element and spectral codes, we have validated the usage of spectral code in this particular situation, where the small transitional region from one fluid density to another may undermine the spectral convergence. In addition to the code–code comparison, we have also performed standard convergence tests on the spectral code when applied to the miscible RT simulation to check the spectral convergence with the presence of a thin interface. We obtain the expected spectral convergence if the interface is smooth and well resolved. The ideal density discontinuity (or, in our case, a sharp temperature jump) cannot be resolved in spectral codes without special treatment; we therefore use a hyperbolic tangent or an error function for the background temperature field to make sure that the initial temperature field is smooth. From the smoothness of the interface, we obtain spectral convergence as long as we resolve the interface. Figure 1(*b*) shows the spatial convergence of the spectral code when we fix the interface thickness and use a single-mode perturbation as the initial condition. The convergence test for the spectral-element code is conducted separately for the Orr–Sommerfeld equation as shown in table 1. The convergence is non-monotonic due to the fact that the growth

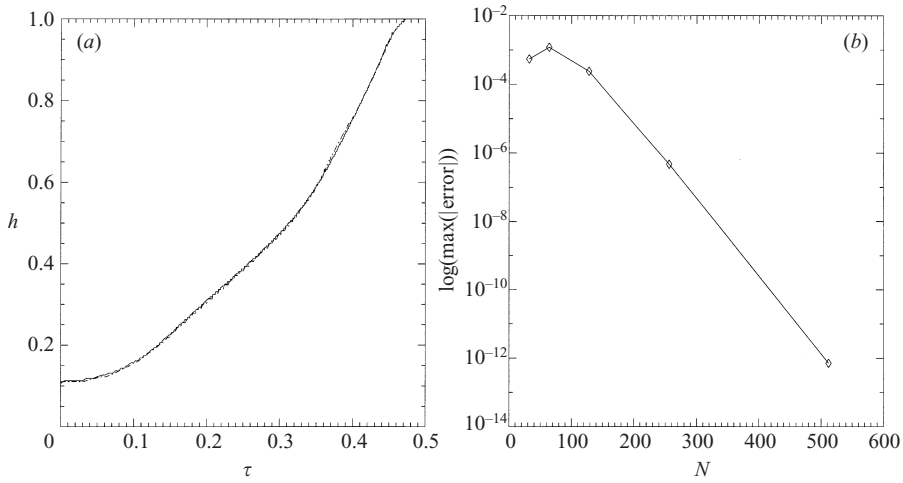

FIGURE 1. (*a*) Comparison between the spectral-element code (solid line) and the spectral code (dashed line) for simulation of a single-mode perturbation at the interface. Plotted is the mixing zone width h as a function of time τ. (*b*) The spectral code shows exponential convergence for a fixed interface thickness of 0.15 in the single-mode simulation. The error is defined as the deviation from the simulation with a resolution of 1024.

N	$E(t_1)$	$error_1$	$error_g$
7	1.11498657	0.003963	0.313602
9	1.11519192	0.003758	0.001820
11	1.11910382	0.000153	0.004407
13	1.11896714	0.000016	0.000097
15	1.11895646	0.000006	0.000041

TABLE 1. Spatial convergence of the spectral-element code for the Orr–Sommerfeld problem: $K = 15, \mathrm{d}t = 0.003125$. $E(t_1)$ is the energy of the perturbation at $t_1 = 25.1437$, the one period of oscillation for the TS wave. $error_1$ is the error in energy when compared to theory, and $error_g$ is the error in growth rate.

rates oscillate about the analytical value. However, spectral convergence is clearly attained.

Having demonstrated the validation of the spectral code, we present results from simulating the system with the spectral code in the rest of the paper. We adjust both the resolution and the interface thickness so that there are enough grid points across the background temperature profile.

3. 'Random' perturbations at the interface: two versus three dimensions

In this section, we focus on the consequence of perturbing the interface with a spatially randomized disturbance. The initial perturbation imposed at the interface in the three-dimensional simulation is shown in figure 2. This perturbation is the outcome of phase randomization of a spatial spectral distribution which peaks at $k \sim 8$ and whose bandwidth is approximately 4 centred at the peak. This initial perturbation has been defined as one of the canonical test problems of the 'alpha group' collaboration (A. Cook & G. Dimonte, private communication). The perturbation

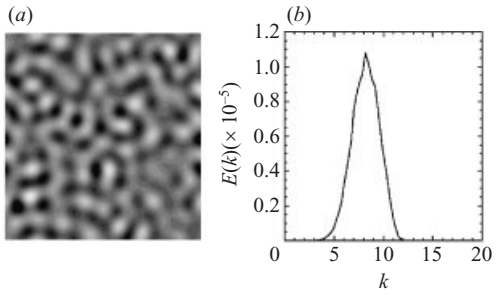

FIGURE 2. Initial random perturbation at the interface ($z = 0.06$): (*a*) the top view of the perturbation and (*b*) the power spectrum of the perturbation.

spectrum (figure 2*b*) is designed so that the fastest growing mode is well resolved for the given resolution ($256 \times 256 \times 512$). The physical motivation for this initial condition is that we want to have 'many' (for our resolution, we have around 60 small plumes at the beginning) well-resolved small plumes seeded at the initial interface to study the mixing of the instability in detail. Later we also show that the growth rate of this mode ($k \sim 8$) is close to the growth rate for non-diffusive, inviscid fluid (figure 9).

We place the position of the initial interface at $z = 0.06$ ($-1 \leqslant z \leqslant 1$), so that we can compare the behaviour of penetrating plumes as they approach the top and bottom walls near the end of the simulations. (From our simulation, we conclude that the effect of the top and bottom boundaries is not important to the propagation of the mixing zone until the mixing zone width reaches $\sim 90\%$ of the box size.) The corresponding initial temperature profile used in the two-dimensional simulations is taken from a planar cut through the three-dimensional initial profile, e.g., the $y = 0$ plane ($T(x, y = 0, z)$) (we also have conducted the two-dimensional simulations with other planar cuts from the three-dimensional profile and found no material differences). In all instances, we treat the case $\nu = 10^{-3}$ and $\kappa = \nu$.

3.1. *Time evolution*

3.1.1. *Mixing zone width*

We first compare the two-dimensional and three-dimensional temporal evolution; the panels in figure 3 show the two-dimensional time evolution of the temperature, while figure 4 shows the time evolution of $y = 0$ slices from the three-dimensional simulations. Figure 5 provides the penetration depths as functions of dimensionless time for two and three dimensions. (To scale our time according to Youngs' time scale (Youngs 1991), we multiply t with $(\beta g/l)^{1/2}$; thus $\tau \equiv (\beta g/l)^{1/2}t$, where l is the half-height of the box). The penetration depth is determined by measuring the distance between boundaries of volume fraction of 1% of the hot fluid and 99% of the cold fluid.

In figure 6 we show how h varies depending on different volume cuts of hot and cold fluids, and we conclude that penetration depths are well defined if the volume cuts are narrower than the 1–99% range, which is what we have adopted to calculate results presented below. We plot the penetration depths against τ^2 instead of τ in order to clarify the scaling behaviour. For both two and three dimensions, $h \propto \alpha\tau^2$ during the early stage of the evolution for $1.8 \leqslant \tau \leqslant 4.4$. The α for this period of time is ~ 0.017 for the two-dimensional case, and $\alpha \sim 0.03$ for the three-dimensional case. Thus, the three-dimensional mixing zone broadens much faster than its two-dimensional counterpart.

FIGURE 3. Time series of the temperature field in a $1(x)$ by $2(z)$ box from the two-dimensional simulations. The interface between cold (black) and warm (white) fluids is perturbed by the $\delta T(x, y = 0)$ slice taken from the spatially random disturbances in the three-dimensional simulations.

We also observe that the scaling range $4 \leqslant \tau^2 \leqslant 12$ is twice the range found in Youngs' work. The mixing zone fills the entire tank at around $\tau = 4.7$ in our case, compared to the values of 2.9–3.1 from simulations with low Mach numbers and high Atwood numbers in Youngs (1991). Finally, we observe that at time $\tau^2 \sim 12$, the increasing h levels off; h then resumes τ^2 scaling at around $\tau^2 \sim 16$; we will discuss this phenomenon in detail in the following subsection. We further remark that the α coefficient for both two and three dimensions presented above is only for early evolution.

3.1.2. *Two-dimensional flows versus three-dimensional flows: finger geometry*

In order to understand these results, we first note that the structure of two-dimensional fingers (plumes) is horizontally stretched, whereas in three dimensions,

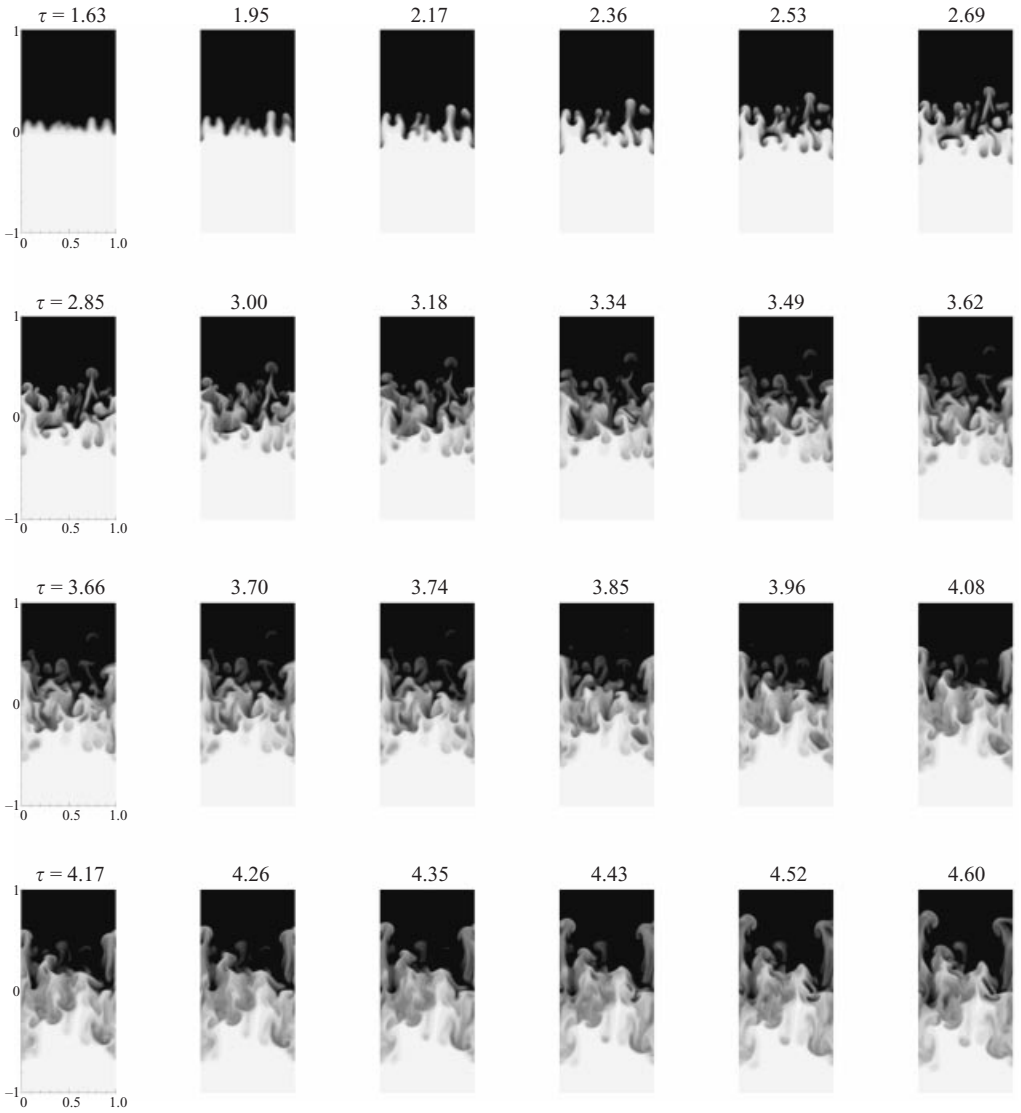

FIGURE 4. Time series of the temperature from the three-dimensional simulations. The slices ($T(x, y = 0, z)$) are taken at the same times as those for the corresponding two-dimensional frames (figure 3).

fingers remain vertical until they merge and form bigger plumes. This implies that the two-dimensional flow has a significantly larger horizontal velocity component when compared to three-dimensional; we return to this observation later when we discuss the evolution of single plumes. In both two and three dimensions, we find one large thermal pushing the envelopes at late times; however, in three dimensions, we observe more local, small-scale structures in the interior of the mixing region than in the two-dimensional case. The large plumes push the edges of the mixing region, and dominate the expansion of the mixing zone at late times. The interior of the mixing zone is also very different between two and three dimensions. In two dimensions, the interior structure is dominated by the large plumes, and therefore

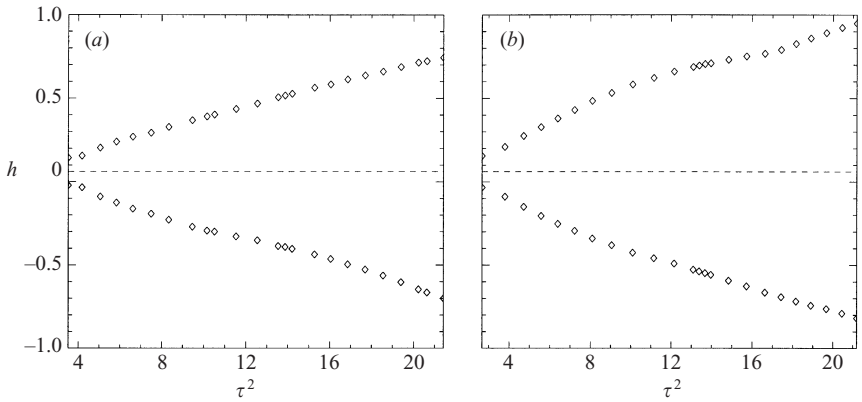

FIGURE 5. Penetration depths from (*a*) two-dimensional and (*b*) three-dimensional simulations for the random perturbation case. For the ascending structures, h is defined as the maximum value where the temperature reaches above 99% of the cold fluid temperature. For the descending mixing zone boundary, h is defined as the minimum value where the temperature drops below 99% of the hot fluid temperature.

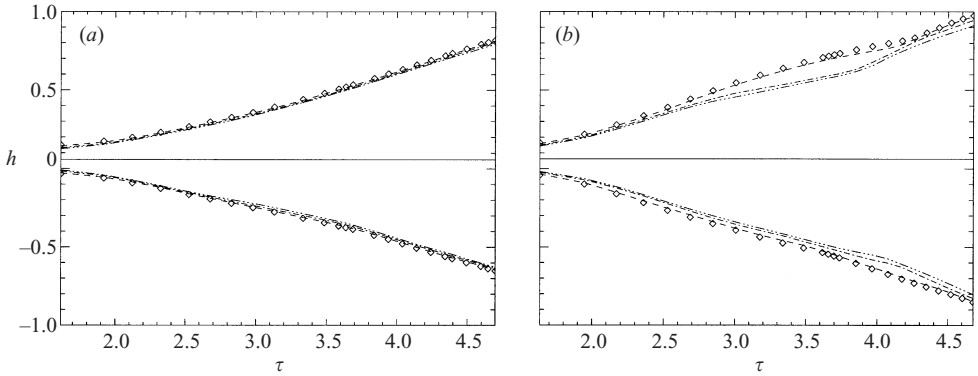

FIGURE 6. Penetration depths from (*a*) two-dimensional and (*b*) three-dimensional simulation for different volume cuts. The two-dimensional curves are from the ensemble average and show similar evolution as in figure 5(*a*). The diamonds are for 0.5–99.5% volume cuts of hot–cold fluids, the dashed lines are for 1–99% volume cuts, the dash-dotted lines are for 3–97% volume cuts, and the dash-dot-dotted lines are for 5–95%.

the general structure of the interior is simple. In three dimensions, the interior is a combination of boundaries between plumes, residuals of mergers, and the wake behind the faster plumes; the interior of the three-dimensional mixing region is thus much more complicated than that of the two-dimensional mixing zone. A simple quantitative measure of this difference in structural complexity between two and three dimensions can be constructed by measuring the stretching of isothermal contours during the course of RT instability. Thus, figure 7 shows the time variation of the isothermal contour length (area) corresponding to $T = 0$ for two (three dimensions). The isothermal contour length is calculated as follows: we first identify points on the isothermal curves, we then calculate the length along the curve by linear interpolation between points. A similar technique has been utilized to calculate the iso-surface in three dimensions.

Initially, the two-dimensional arclength increases much faster than the correspond-

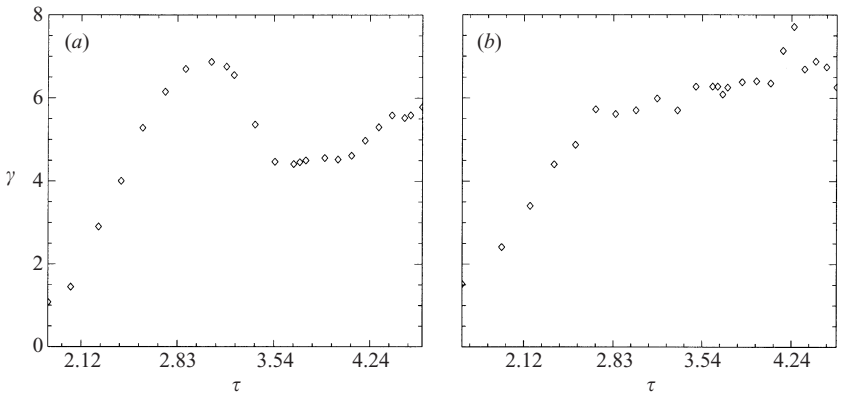

FIGURE 7. Curve lengths of the isothermal contour ($T = 0.0$) for (*a*) two-dimensional and (*b*) three-dimensional simulations.

ing three-dimensional arclength; this is because the two-dimensional isothermal contours are subject to horizontal stretching comparable to their vertical stretching. At late times, however, the two-dimensional isothermal contour breaks off into several connected contours, and thus a sharp decrease in the arclength results. In the three-dimensional case, the arclength increases almost monotonically until a maximum value is reached. This peak is due to the stretching by the shear flow as the edge plumes push the envelopes sideways. The break-off of this isolevel near the front explains the decrease in the arclength at $\tau \sim 4.2$.

3.1.3. *Energetics: two versus three dimensions*

We now focus on the comparison between two-dimensional and three-dimensional energetics: We first plot the ratio of kinetic energy to potential energy available to the flow as a function of time in figure 8. Our results show a remarkable feature: the two-dimensional nonlinear Rayleigh–Taylor instability is more efficient at extracting gravitational potential energy than its three-dimensional counterpart, yet (as shown in § 3.1), the two-dimensional mixing zone grows more slowly than its three-dimensional counterpart. As we will show below, this apparent contradiction is resolved when one looks at how the kinetic energy is partitioned. Youngs (1991), found that the two-dimensional flow is less dissipative than the three-dimensional flow. In his simulations he found that the kinetic energy reaches a maximum at $\tau \sim 6$ for both two and three dimensions. However, the three-dimensional flow is more 'dissipative' and therefore the three-dimensional kinetic energy decreases significantly from the maximum after $\tau = 6$. He also showed that in three dimensions the difference between potential energy and kinetic energy is greater than in two dimensions. This is consistent with our findings. Later we show the energy spectrum of the flow inside the mixing zone from our three-dimensional simulations (figure 15). Similar energy spectrum can also be found in Youngs (1991).

In figure 9 we plot this energy ratio for the three-dimensional case at early times (the two-dimensional growth is almost the same). The growth rate from figure 9 is ~ 8, close to the growth rate (~ 9) for $k = 8$ (where the spatial perturbation spectrum peaks) from the analytic results for the inviscid case (Chandrasekhar 1961). Thus we conclude that the $k = 8$ mode dominates the evolution of the initially randomly seeded perturbation. We also note that at around $\tau \sim 1.3$, which is 6 e-folding times after the initiation of linear growth at $\tau \sim 0.3$, we begin to observe saturation due

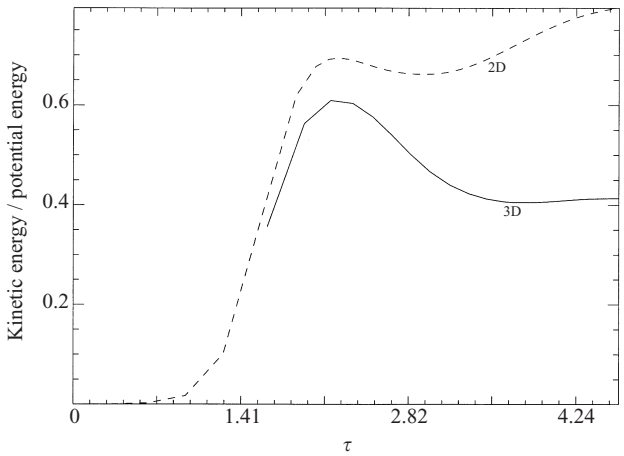

FIGURE 8. Ratio of kinetic energy to gravitational potential energy: two-dimensional versus three-dimensional simulations. The kinetic energy is the volume integral of the kinetic energy density, and the potential energy is the volume integral of the potential energy available in the system. For $\tau \leqslant 1.4$, the growth is exponential and is similar for both two and three dimensions, after this period, two-dimensional motions are much more efficient in extracting potential energy than three-dimensional motions.

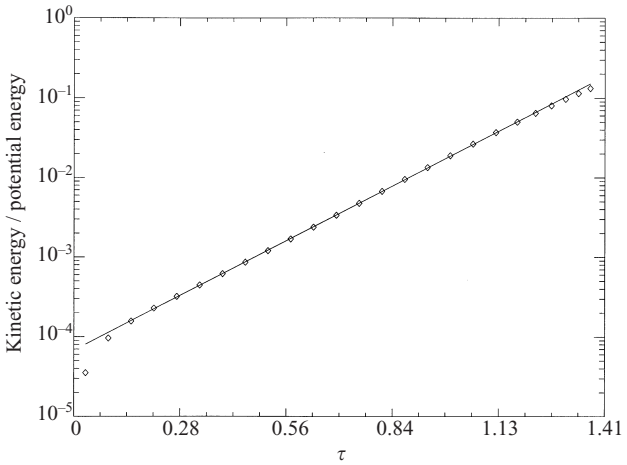

FIGURE 9. Early evolution of the three-dimensional random perturbation. The diamonds are data from the numerical simulation. The solid line is the best fit on the log-linear plot (for $0.28 \leqslant \tau \leqslant 1.13$), and the duration of the linear growth is about 4 e-folding times with a growth rate of 8. The growth rate obtained from the analytic results ($n^2 = gAk$, with $gA = 10$ and $k \sim 8$ from the power spectrum of our initial perturbation at the interface), is 9.

to the nonlinear terms; this marks the beginning of the nonlinear evolutionary stage. After this linear regime, the peak of the spectrum decreases in amplitude and moves toward the small wavenumber end, an indication of formation of large scales.

3.2. *Average quantities and the spatial structure of the mixing zone*

3.2.1. *Average quantities*

Here we focus on the evolution of the horizontally averaged quantities: the horizontal components of the vorticities and the advective thermal fluxes $\boldsymbol{u}T$; after horizontal

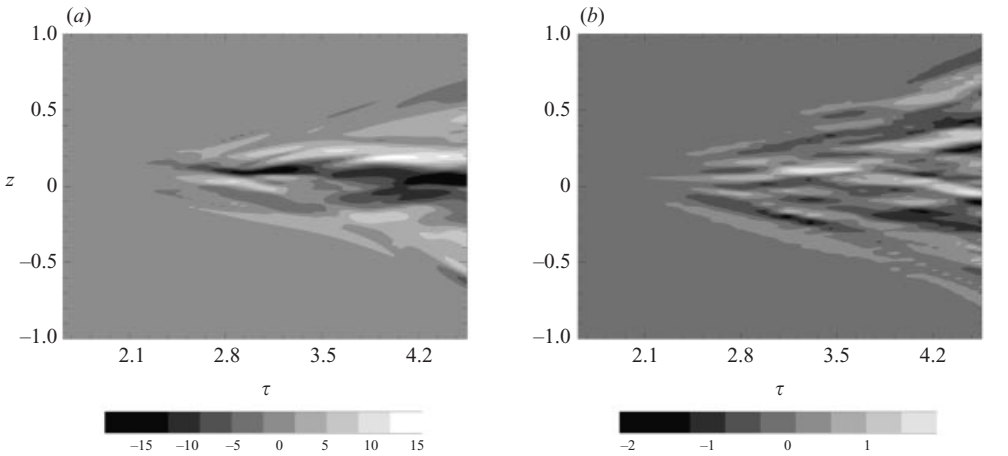

FIGURE 10. Horizontally averaged vorticity as functions of z and t: (a) the two-dimensional vorticity, (b) the mean horizontal three-dimensional vorticity components.

averaging, each of these quantities is only a function of the vertical coordinate (z) and time (τ). We note that the buoyancy flux is the vertical component of the advective flux, while the buoyancy gradient is the vertical component of the thermal gradient.

First, we concentrate on the average horizontal components of the vorticity (figure 10). The average of the horizontal vorticity is basically the vertical gradients of the horizontal components of the velocity, as we adopt periodic boundary conditions in the lateral directions. We note that the amplitude of the two-dimensional vorticity is almost 5 times larger than that of the three-dimensional vorticity components. The evolution of the two-dimensional vorticity (panel a) is indicative of the strong shear strength at the centre of the mixing region. The patches of interchanging shades of grey in the time–space plot of the three-dimensional vorticity components (figure 10b) indicate the merging events within the mixing region. We observe a similar pattern in the plot of two-dimensional vorticity, but only at early times; at late times, the two-dimensional space–time plot is more indicative of the roll-up of big thermals.

In figure 11 we show the time–space plot of the average advective thermal fluxes in the horizontal and vertical directions; the corresponding three-dimensional plots are shown in figure 12. We note that in two dimensions, the two fluxes are comparable in amplitude, whereas in three dimensions, the horizontal advective fluxes are of comparable amplitude yet are both smaller than the vertical flux (buoyancy flux) by a factor of 5. This is a manifestation of the fact that the three dimensional flow is dominantly in the preferred (i.e. vertical) direction, while the corresponding two-dimensional flow is strongly sheared (and has comparable magnitude in the horizontal and vertical directions). The space–time plots for the diffusive thermal fluxes basically reveal the same broadening structure of the mixing zone. The horizontal components in two and three dimensions are comparable, and the two-dimensional vertical diffusive flux is larger than the three-dimensional vertical flux, as found in the average advective fluxes.

To briefly summarize: we observe stronger two-dimensional vorticity generation compared to three-dimensional; consequently, we observe that the two-dimensional horizontal transport is much more effective than the three-dimensional; the relative efficiency of vertical advective transport to horizontal transport, in contrast, is much higher in three dimensions than that in two dimensions.

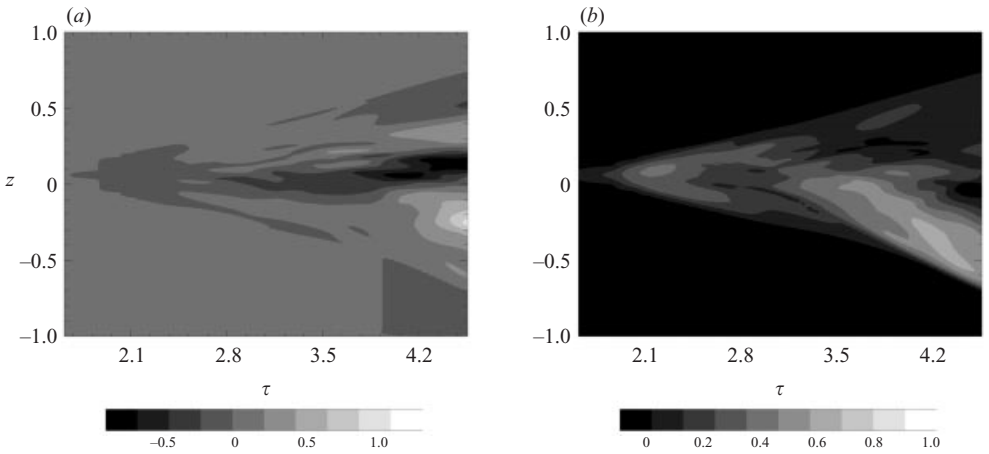

FIGURE 11. Average advective fluxes (two-dimensional) as functions of z and t: (a) the horizontal flux and (b) the vertical (buoyancy) flux.

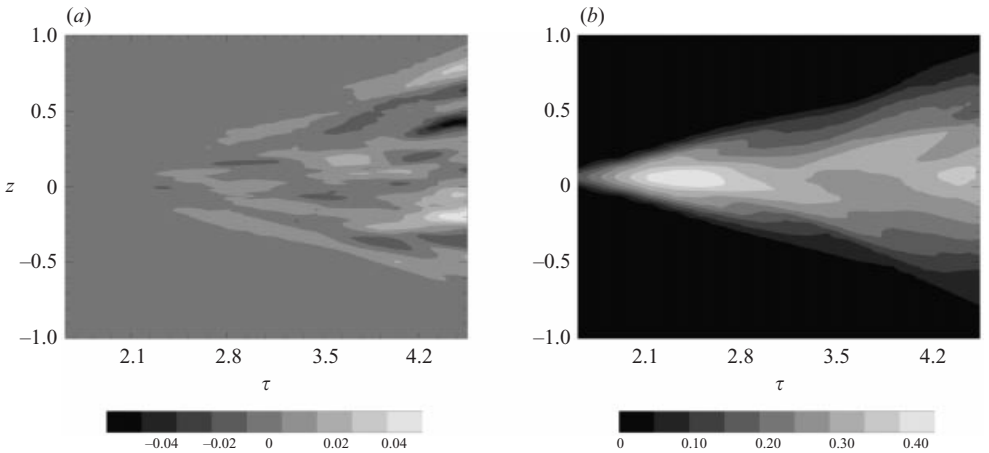

FIGURE 12. Horizontally averaged advective fluxes (three-dimensional) as functions of z and t: (a) the mean horizontal components and (b) the vertical (buoyancy) flux.

3.2.2. *Turbulence and mixing within the mixing zone*

As shown in the time series for both two and three dimensions, the spatial structure of the two-dimensional mixing zone is relatively much simpler than the three-dimensional: the two-dimensional mixing zone is dominated by one or two big plumes while in three dimensions the centre of the mixing zone is full of small-scale structures. This is clearly manifested by the temperature fluctuation probability distribution function (PDF) within a thin horizontal slice of the three-dimensional mixing zone. In our analysis we find that a thickness of $\Delta z = 0.06$ (the initial interfacial thickness) suffices to provide good statistics for the PDF. If we place this thin slice at the position of the initial interface, we find the PDF of the temperature fluctuations ($\Delta T \equiv T - T_0$) to be a Gaussian centred at $\Delta T = 0$ (figure 13). As we move this thin slice away from the initial interface, the PDF transitions from a Gaussian distribution to an exponential distribution (figure 14). Moving further than 1/3 of the mixing zone width from the centre, the PDF of the thin slice transitions again from an exponential distribution to

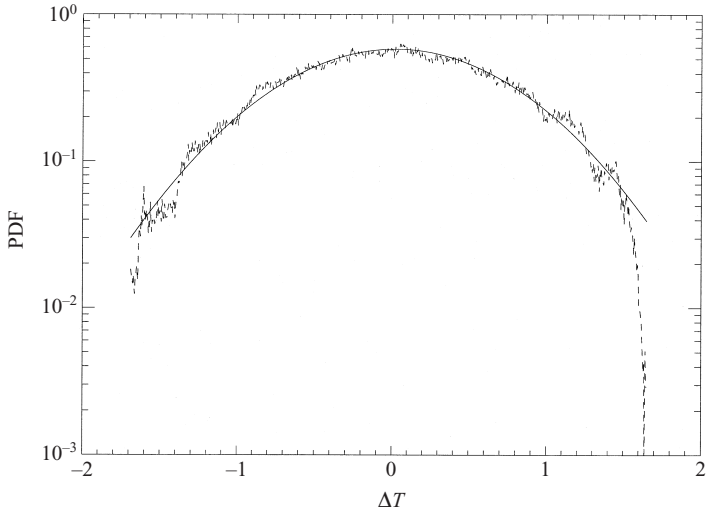

FIGURE 13. PDF of the temperature fluctuation ($\delta T = T - T_0$) within the mixing zone ($\Delta z = 0.025$) at the position of the original interface ($z = 0.06$).

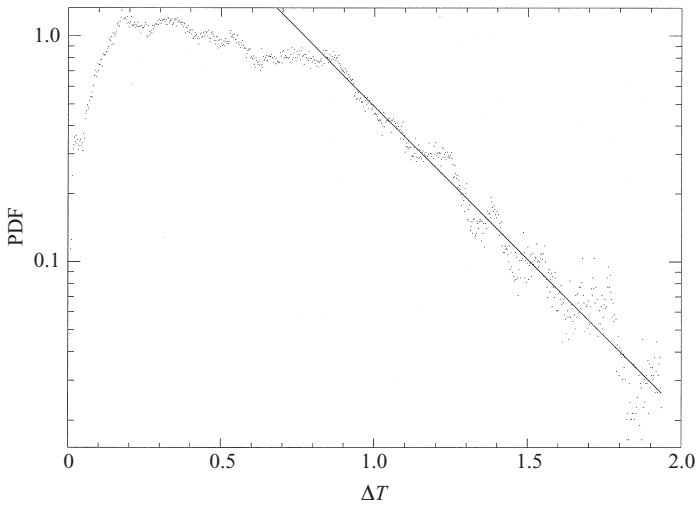

FIGURE 14. PDF of the temperature fluctuation ($\delta T = T - T_0$) within the mixing zone ($\Delta z = 0.025$) at $z = 0.21$.

a yet steeper distribution (more like a delta function centred at either -2 or 2). The Gaussianity in the scalar PDF at the centre of the mixing zone (figure 13) implies turbulent mixing of the scalar near the centre. For the flow inside the mixing zone, the direct evidence for turbulence is a $-5/3$ Kolmogorov energy spectrum. Due to our numerical resolution ($256 \times 256 \times 512$) the scaling range is small as shown in figure 15, where the energy spectrum shows an inertial range from $k \sim 4$ to $k \sim 18$.

As we move from the centre of the mixing zone towards the boundary, the exponential PDF of the scalar at $z = 0.5$ implies that the flow that mixes the scalar is dominated by large scales. This indicates that, for the miscible RT instability and the parameters that we explore, turbulent mixing exists only near the initial interface,

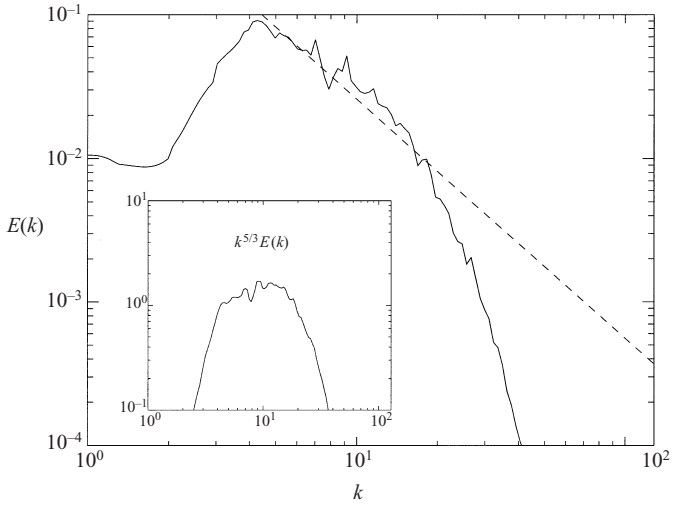

FIGURE 15. Energy spectrum of the flow at the end of the simulation. The dashed line is the Kolmogorov $-5/3$ scaling. The inset shows that the inertial range is from $k \sim 4$ to $k \sim 20$.

and that most of the mixing zone is still dominated by finger structures. These finger structures (plumes) near the edge are responsible for the broadening of the mixing zone. As we will show in § 5, the propagation speed of a plume in an ambient environment is directly proportional to its circulation. Also shown in § 5 is that, if the drag is small, these plumes initiated by the perturbation at the RT interface will be free falling (rising) without any turbulent scaling involved. Furthermore, if the plumes pushing the edge of the mixing zone experience a different flow in the background, we would expect a different mixing zone broadening. For example, if the horizontal components of the flow are comparable to the vertical component, we expect the propagation of the mixing zone to slow down. Therefore, the transition of the ambient background flows would serve as an indication of deviation from the free-falling phase of the mixing zone. In the next subsection we will provide evidence for alteration of flow patterns inside the mixing zone in the three-dimensional case. Combining all the results, we are able to demonstrate the correlation between the transition of the interior flows and the transition of the mixing zone broadening.

3.3. *Mixing zone broadening and the internal flow structures*

We now focus on the relationship between the propagation of the mixing zone and the internal flow structures at around $\tau^2 = 10$ in the three-dimensional case. In figure 16 we show the average horizontal and vertical components of viscous dissipation rate: the horizontal component is simply $v(u_1\nabla^2 u_1 + u_2\nabla^2 u_2)/2$ and the vertical component is $v(u_3\nabla^2 u_3)$. In figure 17 we show the ratio of the volume integral of these two components.

Some observations from these results can help us gain insight into the mixing zone evolution: we note that average buoyancy flux (figure 12*b*) reaches maximum at $\tau \sim 2.3$, while the average vertical component of the dissipation rate (figure 16*b*) reaches maximum around $\tau \sim 2.8$. Just after $\tau = 2.8$, we observe generation of vorticity inside the mixing zone, as shown in figure 10(*b*). Moreover, the horizontal component of the advective fluxes (figure 12*a*) starts to develop structures around $\tau = 2.8$ as well.

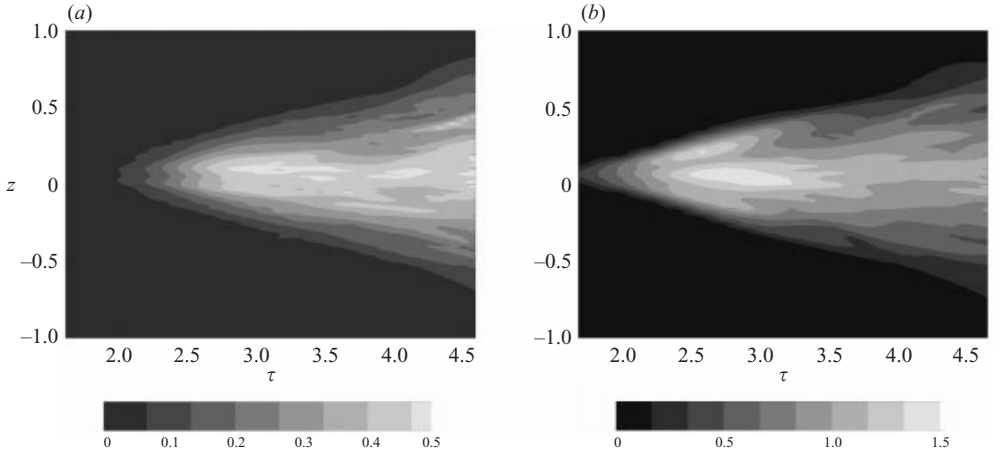

FIGURE 16. Average viscous dissipation rates as functions of z and t: (a) the dissipation rate due to the horizontal components of the flow, and (b) the vertical component.

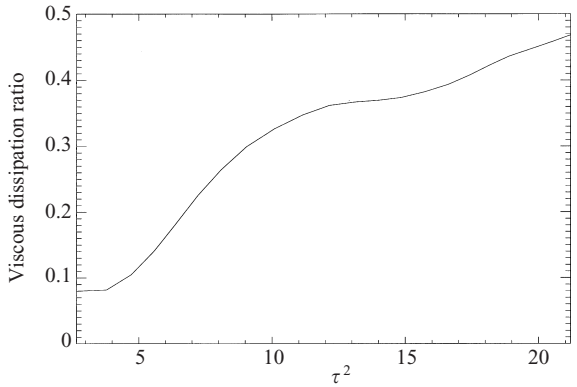

FIGURE 17. Ratio of the horizontal component to the vertical component of the volume-integrated viscous dissipation rates as a function of time (τ).

We can now summarize the evolution of the three-dimensional RT instability as follows. As the interfacial random perturbations initiate some circulation (small vortices), the seeded vortices increase in strength and begin free falling, accelerated by the density contrast across the interface (as we discuss further below). This is the free-falling phase, where the mixing zone is expanding due to a constant acceleration at the boundaries, and inside the mixing zone, the interaction between vortices is not strong enough to alter the free-falling dynamics. At $\tau^2 \sim 8$, the dissipation rate begins to increase at a lower rate as a result of increasing mixing inside the mixing zone. The development of structures is most vigorous as the horizontal flow is enhanced and the viscous dissipation rate plateaus at $\tau^2 \sim 10$. Hence we mark $\tau^2 = 10$ as the beginning of the mixing phase. From figure 17, we also observe that the end of the mixing phase can be identified at $\tau^2 \sim 16$, when the viscous dissipation rate resumes positive growth. The existence of this mixing phase also manifests itself in the potential energy release rate and the kinetic energy partition (figure 18). The potential energy release

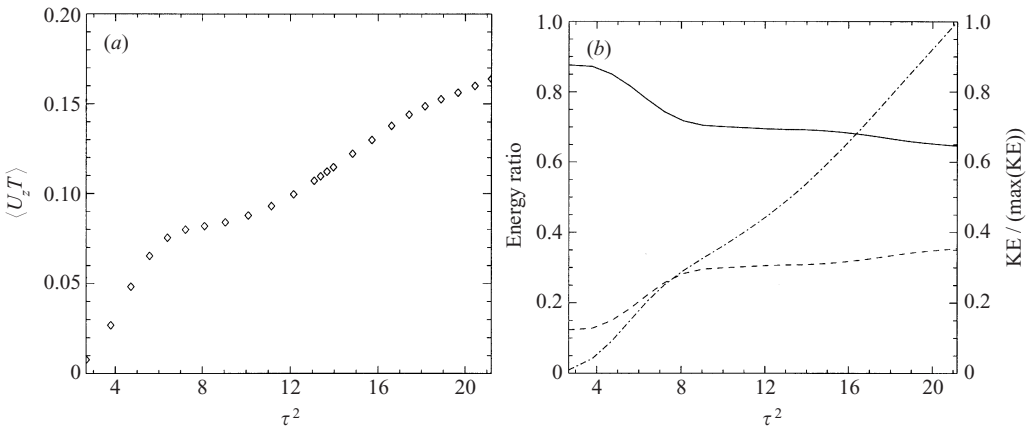

FIGURE 18. (*a*) Volume-averaged advective fluxes as a function of time. (*b*) Partition of kinetic energy as functions of time; the solid line is the partition of the kinetic energy in the vertical direction and the dashed line is along the horizontal directions; the dash-dotted line is the normalized kinetic energy.

rate is defined as the volume-averaged, vertical advective flux as follows:

$$\int_{\Omega} wT \,\mathrm{d}^3x = \partial_t \int_{\Omega} zT \,\mathrm{d}^3x + \kappa T|_{z=-1}^{z=1}. \tag{3.1}$$

(We have utilized no-flux boundary conditions in deriving the above equation.) The last term on the right-hand side is negligible for small κ, as the temperature difference is always of order one in our simulation. In figure 18(*a*), we observe that just before the beginning of the mixing phase the potential energy release rate reaches a plateau. In figure 18(*b*), the partitions of kinetic energy remain more or less constant throughout the mixing phase, after which they resume their original direction of variation with time. Thus we conclude that this mixing phase ($10 \leqslant \tau^2 \leqslant 16$) is a regime where horizontal components amplify and the lateral transport is also enhanced in the flow. After this stage, the boundary of the mixing zone is not pushed outward by a collection of plumes of the smaller sizes as in the free-falling phase, but by a small number of big plumes that manage to survive the mixing phase and expand in size as they propagate outwards. It is therefore important for us to understand the evolution of plumes and their propagation in various kinds of ambient background flows.

We also note that, based on our discussion, we expect to see departures from simple τ^2 scaling only when the dynamics is dominated by a small number of (larger) plumes. As a consequence, the aspect ratio of the experimental domain can be decisive in determining whether such departures are actually observed: as the height-to-width ratio decreases, we expect to see departures from τ^2 scaling at later and later times, so that plumes may begin to interact with the box walls before such departures can be observed. Thus we conclude that the dynamics and evolution of single fingers (plumes) are important to the broadening of the mixing zone in both two- and three-dimensional RT instability. In the following sections, we first discuss RT models based on the point sources and interactions between each source. We will introduce the buoyancy–drag plume model in the context of the existent point source models, and uncover the connections between these models based on the physical grounds.

4. Models for RT instability

Early analytic work on modelling the mixing zone broadening goes back to Fermi (1951) (see also Sharp 1984); more recent models can be found in Alon, Shvarts & Mukamel (1993) and Alon *et al.* (1994). From the numerical simulations of the random-perturbation cases, we observe that plumes near the edge of the mixing zone are responsible for the broadening. We also observe that for the parameters we adopt for our simulations, the interior flow of the mixing zone is not homogeneous and is not isotropic. Instead, the flow pattern inside the mixing zone has a preferred direction associated with the plume structure inside the mixing zone and cannot be described as fully developed turbulence. Motivated by these observations, we focus on RT models that do not require the existence of turbulence to achieve the free-fall scaling. We first briefly summarize two such models for immiscible RT instability: the first is for strongly stratified RT instability ($A = 1$); the second is for weakly stratified RT instability ($A \to 0$). The similarities between these two models (as will be shown) lead one to conjecture that there may exist a point-source model that incorporates both limits. Indeed, the long-existing buoyancy–drag model, often used in modelling thermals or plumes, seems to capture the essential physical features in both models; and we will argue that this model provides an adequate framework for capturing the essential physics of nonlinear RT instability. We will discuss this third model at the end of this section.

4.1. *Two models: bubble competition model* ($A = 1$) *and point source model* ($A \to 0, Ag$ *fixed*)

Zufiria's bubble competition model (Zufiria 1987) assumes a two-dimensional potential flow model with an Atwood number of 1. In essence, this model is an extension of Wheeler's model (Sharp 1984) to the strongly stratified limit. The model consists of variables that quantify the internal potential flow within each bubble (point source inside the bubble) and the distances of the source of the internal flow to the bubble boundaries (radii of curvature of the bubble). For a system of 20 bubbles at the beginning, an estimated range $0.04 \leqslant \alpha \leqslant 0.07$ is obtained from this model.

A different model for two-dimensional inviscid, but weakly stratified RT instability, is given by Aref & Tryggvason (1989). This model focuses on the Boussinesq limit, i.e. $A \to 0$ and Ag remains constant. Following Tryggvason (1988), the inviscid two-dimensional Boussinesq RT instability is formulated in terms of vortex sheet strength across the density interface. Vortex sheet strength, defined as the difference of the tangential velocity along the interface per unit length, is driven by the density contrast across the interface. In their model, they are able to capture the complicated vortex pair evolution with a simple evolutionary equation for the circulation per arclength. They also successfully extend the single vortex pair model to multi-vortex-pair systems, and the initial linear growth rate from their model is in fair agreement with the analytic results.

4.2. *Relating the models: the buoyancy–drag model*

As pointed out by Aref & Tryggvason (1989), their vortex model is similar to the bubble-competition model: the point source in the bubble model corresponds to the point vortices in the vortex model, and the radii of curvature of the bubble correspond to the vertical coordinates of the point vortices in the vortex model. The striking similarities stem from the fact that bubbles, especially ones elongated in the stratified direction, have flow patterns that amount to a vortex ring near the elongated end and a point source inside the bubble feeding the vortex ring. Therefore,

the buoyancy–drag model used in modelling plumes or thermals seems to be a natural candidate to connect the bubble picture, where point sources are driven by a strongly stratified density contrast across the interface, to the vortex picture, where the point sources are driven by infinite gravitational acceleration (with Ag constant).

The most simplified buoyancy–drag model (Lighthill 1986; Werne 1994) describes the propagation velocity (V) of a plume as follows:

$$\frac{\mathrm{d}(\rho_{in}V)}{\mathrm{d}t} = \delta\rho\,\alpha g - C_D\rho_{out}V^2, \tag{4.1}$$

where αg is the effective acceleration due to the buoyancy contained by the thermals to drive the motion, $\delta\rho \equiv \rho_{out} - \rho_{in}$ is the density contrast between the inside and outside of the thermals, and C_D is the drag coefficient which depends on the geometry of the thermals and the fluid viscosity. There are more elaborate forms of equation (4.1), such as different forms for C_D, but the most essential feature is that if the correction term to the constant acceleration is small when compared to the acceleration, free-fall scaling is naturally obtained. Other variant forms of this simple model have been applied by Kane & Arnett (1998) and Dimonte & Schneider (1999) for a variety of parameters such as Atwood number and Mach number, and the value of α is claimed to be satisfactorily in agreement with results from either experiments or numerical simulations. In the next section, we perturb the RT interface with small, initial vortices: such perturbations generate single plumes expanding in size as they propagate away from the interface. As will be shown, such plumes are well described by equation (4.1). By comparing the propagation velocity with the circulation of the vorticity, we are able to connect the point vortex model to the single plume model. We are also able to explain differences between two-dimensional and three-dimensional miscible RT instability (either the random cases in § 3 or the single plume cases in § 5) by conducting simple energetic diagnostics on the single plumes.

5. The evolution of plumes

The above discussion of the buoyancy–drag model for the nonlinear development of the Rayleigh–Taylor instability, and the observation of Rayleigh–Taylor 'fingers' in the experiments (§ 3), strongly suggests an analogy between the finger structures in the miscible version of the instability and the evolution of isolated thermals or plumes. These latter structures have been investigated extensively in the past (Turner 1973). Experimentally, a bubble of hot fluid is injected near the bottom of a container; the resulting buoyant plume expands as it rises and moves away from the source. Moses, Zocchi & Libchaber (1993) have explored various situations, which include injection of plumes into a turbulent flow. Experimental observations show that as a localized source of buoyancy is injected into the fluid, the resulting convection pattern consists of a cap which forms at the outwards propagating front, and a stem which connects the cap and the local source (Moses *et al.* 1993). In the case of the miscible RT instability, the perturbation at the interface serves equivalently as an injection of buoyancy sources (or sinks) into colder (hotter) fluids. The early development of the perturbation then resembles a collection of plumes going up and down from the interface (figure 19).

As shown in this figure, each rising and falling bubble has a well-defined cap and a stem connecting the cap to the root at the interface, consistent with expectations for the behavior of plumes.

We have numerically simulated plumes which are initiated by perturbing a

FIGURE 19. Plume structures at the early development of miscible Rayleigh–Taylor instability. Initially a layer of cold fluid (black) is on top of a layer of warm fluid (white), and a random perturbation is imposed at the interface.

Run number	βg	$\nu \times 10^3$	$\kappa \times 10^3$	d	a	Aspect ratio
1	2.5	0.5	0.5	0.1	0.14	0.2 : 1
2	2.5	1	1	0.1	0.14	0.2 : 1
3	2.5	1	0.5	0.1	0.14	0.2 : 1
4	2.5	0.5	0.5	0.1	0.11	0.2 : 1
5	2.5	1	1	0.1	0.11	0.2 : 1

TABLE 2. Parameters for single-plume simulations; d is the interface thickness, and a is the amplitude of the perturbation.

Rayleigh–Taylor interface with a vortex pair in two dimensions or a single vortex ring in three dimensions. Our interest is primarily in plume propagation, the temporal development of the detailed geometry of the plumes, the dynamics and energetics of the plumes, and the dimensionality of the plumes. We remark in passing that two-dimensional plumes are referred to as planar vortex pairs in three dimensions, i.e. three-dimensional plumes in which all motions are restricted to lie in parallel, vertically-oriented planes.

In the following, we first establish a connection between miscible RT vortex pairs and the immiscible version (Tryggvason 1988) by comparing the dynamics and the detailed vortex structures. We then present results of two-dimensional simulations (with parameters listed in table 2), and then go on to compare these results with the corresponding results for three-dimensional calculations. The parameters for our single plume simulations are listed in table 2. The two-dimensional plumes are planar, while the three-dimensional plumes have cylindrical geometry. The initial perturbation imposed at the interface is a Gaussian wave packet with amplitudes listed in table 2.

5.1. *Two-dimensional single plumes*

5.1.1. *Connection to weakly stratified, immiscible RT instability*

Tryggvason (1988) utilized the vortex sheet strength to describe the evolution of single-mode perturbations in two-dimensional immiscible RT instability. In the case of miscible RT instability, one can construct a family of isothermal contours due to the diffusivity; we can monitor the evolution of single plumes by evaluating various quantities (such as vorticity, thermal flux) on the isothermal (or, in Boussinesq fluids, isodensity) contours. As long as the structure of the isothermal contours remains relatively simple (as shown in figure 20*a*), we can gain some understanding of the structure of the buoyant plumes by considering the evolution of various physical quantities along the isothermal surfaces. Figure 20 shows the spatial structure of the planar vortex pair for the first set of parameters in table 2. The roll-up structure is reminiscent of those observed in the weakly stratified, immiscible RT instability (Aref

& Tryggvason 1989). To make complete comparison, we first introduce the circulation (Γ) along some closed curve: The circulation Γ, defined as the line integral of the flow along a closed curve,

$$\Gamma \equiv \int_C \boldsymbol{v} \cdot \mathrm{d}\ell, \tag{5.1}$$

is related to the evolution of vortex pair as follows:

$$\frac{\mathrm{d}\Gamma}{\mathrm{d}t} = \int\int_A \nabla\frac{1}{\rho} \times \nabla p \cdot \mathrm{d}\boldsymbol{A}, \tag{5.2}$$

where $\boldsymbol{A}$ is the surface enclosed by the curve $\boldsymbol{C}$. In the case of weakly stratified Rayleigh–Taylor instability (Aref & Tryggvason 1989), the above relation is modified by replacing the right-hand-side integral with the potential energy density due to the interfacial density contrast. The propagation velocity (V) of the vortex pair in a non-stratified fluid is then related to the circulation Γ as

$$V = \Gamma/\eta, \tag{5.3}$$

where η is basically the correlation length for vortices, and is a function of geometry and dimensionality: one expects η for two-dimensional vortex pairs to be larger than for three-dimensional vortex rings. Equation (5.3) is valid even in the case of weakly stratified RT instability, where vortices, originally initiated at the interface due to the density perturbation, propagate in a uniform ambient background.

With equation (5.3), we can connect the bubble model to the point vortex model via the buoyancy–drag plume model. To fix ideas, we first outline an evolutionary scenario for the weakly stratified, miscible RT instability: as we disturb the interface with some temperature perturbation, vortices are generated as a result of lateral thermal gradient. Thus some initial circulation is seeded inside the vortices and a propagation velocity is acquired according to equation (5.3). The circulation then evolves according to equation (5.2), and the propagation velocity is approximately given by equation (5.3) at each time step for an updated circulation (Hill 1975). We also observe that the acceleration experienced by the vortex pair is proportional to the increase/decrease in rate of change of circulation Γ. Combining equations (5.2) and (5.3), we obtain the equation for the acceleration for the planar vortex pair:

$$\frac{\mathrm{d}V}{\mathrm{d}t} = \frac{\mathrm{d}(\Gamma/\eta)}{\mathrm{d}t} = gf(\delta\rho, \hat{\boldsymbol{s}}), \tag{5.4}$$

where g in equation (5.4) is the gravitational acceleration, and f is a function of density contrast ($\delta\rho$) and geometry of the interface (unit tangent vector along the interface $\hat{\boldsymbol{s}}$).

For point vortices (Aref & Tryggvason 1989), $f = \hat{\boldsymbol{g}} \cdot \hat{\boldsymbol{s}}$ where $\hat{\boldsymbol{g}}$ is the unit vector along the gravitational direction and $\hat{\boldsymbol{s}}$ is the unit tangent vector along the interface. In our case, we expect f to be a constant (effective acceleration) plus some correction term due to viscous drag. This expectation arises from two facts. The first is the observation that the plume consists of a vortex pair inside the cap and a flow sustaining the vortex structure (the neck connecting the cap to the stem). Therefore, we expect the dynamics of the vortex pair to be similar to the plume dynamics. The second fact is that the propagation of buoyant plumes (not sustained by a constant source) in a homogeneous fluid is described by the buoyancy-drag model (equation (4.1)), where the constant density difference across the plume boundary provides buoyancy acceleration, and the viscous drag experienced by the plume causes a

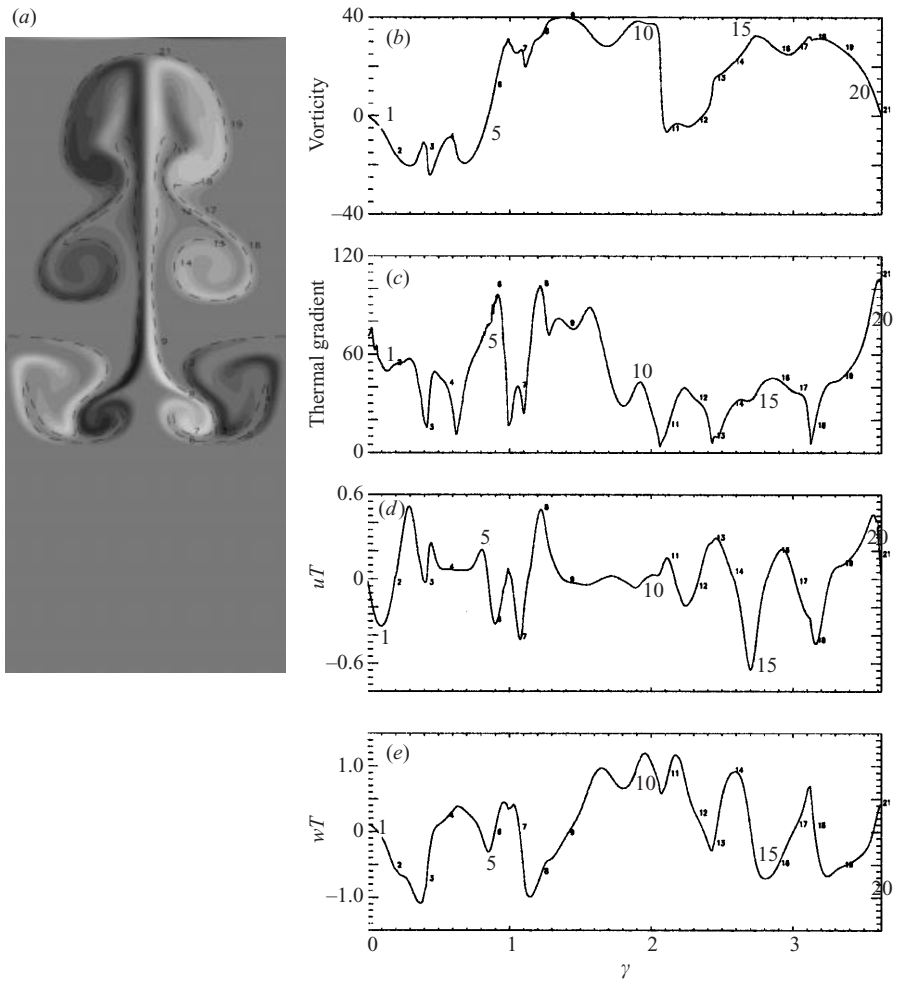

FIGURE 20. (*a*) Two-dimensional vorticity contour plot and (*b–e*) the value of various physical quantities along the $T = 0.75$ isothermal curve: (*b*) vorticity, (*c*) the projection of the thermal gradient on the isocurve, (*d*) the horizontal heat flux and (*e*) the vertical heat flux are evaluated along the isocurve. For illustration, we place numbers along the isocurve to display the important spatial features related to the flow pattern.

deceleration. To be more specific, we expect f to take the following form:

$$f = \alpha + \gamma(v, \delta\rho, V), \tag{5.5}$$

where the 'constant' α may depend on the dimensionality and the initial perturbation, and the correction terms are included in the function γ (a function of viscosity v, the propagation velocity V and the density difference $\delta\rho$). If γ is chosen to be proportional to $-V^2$ as in Werne (1994), the propagation velocity will reach a constant terminal velocity ($V = V_f$ is a constant) after a free-falling period ($V \propto t$ and $h \propto t^2$).

To fully establish the correspondence between the immiscible point vortex model and the miscible plume model, we calculate the circulation Γ along isothermal contours (not necessarily closed) in our two-dimensional simulations. Figure 21(*a*) shows the temporal evolution of Γ along $T = 0.7$, and during $0.7 < \tau < 2.1$, we find Γ to be proportional to τ^2. Comparing with figure 21(*b*), we note that this duration

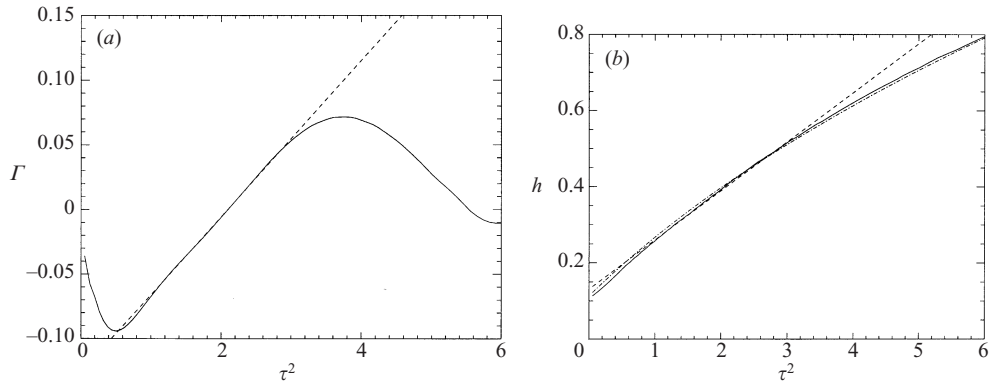

FIGURE 21. Circulation Γ (along the $T = 0.7$ isothermal contour) and the propagation of a two-dimensional single plume. In (*a*), the solid line is from the simulation, and the dashed line is the τ^2 fit. In (*b*), the solid line is from the simulation, the dashed line is the τ^2 fit, and the dash-dotted line is the fit to the single plume model.

coincides with the free-falling phase when h scales with τ^2. This is similar to what is observed in Aref & Tryggvason (1989): the propagation of the two-dimensional vortex pair is free-falling at the beginning, and it decelerates due to the decrease of available potential energy per unit arclength as the rollup continues (and also due to diffusion and viscous dissipation in our case) – thus the decrease in circulation inside the vortex pair. We also note that the constant initial acceleration rate of Γ even in the miscible case indicates that the initial circulation is due to the buoyancy-driven flow around the cap head. As the circulation increases, drag becomes important and the circulation saturates to a maximum. The circulation then decreases at late times due to the strong enhancement of the horizontal motion, which is typical of two-dimensional flow and less so in three-dimensional flow (we will discuss this difference later). We should point out here that, despite the similarities already presented between the point vortex model and plume model, there exists an essential difference: the plume has a stem structure associated with the circulation around the neck, which closely resembles the flow in the vicinity of RT 'fingers'. Our future research problem is to understand how the presence of multiple plumes affects the circulation near the necks; this will be an important future step in connecting these models to the RT finger evolution in more vigorous flows (higher Reynolds numbers).

We are now ready to compare the vortex structure between the miscible RT instability and the immiscible version. From figure 20(*b*), we make the following observations:

(i) The vorticity vanishes at the tip of the cap head. This implies that the flow near the cap is essentially irrotational, and explains why the potential flow assumption adopted in the derivation of the cap shape by Lighthill (1986) (see also Moses *et al.* 1993) works so well in describing the head shape. This is also consistent with results for the weakly stratified, inviscid RT instability (Aref & Tryggvason 1989; Tryggvason 1988).

(ii) The vorticity reaches extrema near the neck of the plumes, i.e., near the part of the plume which connects the stem and the cap head; this is the location where circulation is most vigorous. This is also consistent with the fact that circulation reaches an extremum at the inflection points along the interface (Aref & Tryggvason 1989).

(iii) The amplitude of the thermal gradient reaches extrema either near the cap heads or near the neck of the plumes. This is consistent with the previous observation, because the larger the thermal gradient is, the larger the rate of circulation is, and thus the vorticity reaches extrema at these points.

5.1.2. *Dynamics and energetics of two-dimensional plumes*

In this subsection, we study the details of the single plume structures to uncover the physical ingredients essential to model the RT fingers. As in the point vortex model, we find the evolution of arclength of isothermal contours to be indicative of the detailed evolution of the plume structures. Here we first focus on the evolution of the isolevels associated with single plumes. Secondly we explore the dependence of the single plume evolution on the various parameters such as the amplitude of the perturbation, the Reynolds number and the Prandtl number.

Figure 22 is an example of how the arclength evolves as a function of time for different levels from the two-dimensional simulation (run number 4 in table 2), showing the time evolution of arclength for 15 different isothermal contours. These various evolutions in the isothermal contours can shed light on the detailed, local structure of the fluid. First we observe that, among all the 15 curves, curve 11 ($T = -0.4$) has the longest curve length. Curves 1–6 correspond to isolevels near the boundary between the plume and the ambient fluids. Before $\tau \sim 1.0$, the flow inside the plume pushes these levels upward as the plume rises. From $\tau \sim 1.0$ on, these contour levels begin to catch up with the ascending boundary of the plume to the heavy fluid, and the level sets break up into several smaller connected loops. After this event (at $\tau \sim 1.4$), the plume has established its own shape and the cap propagates in a shape-preserving fashion. At time $1.7 < \tau < 2.1$, small vortex pairs near the original interface begin to roll up to bigger vortex pairs and thus the increase in arclength. Curves 7–11 represent transition contours inside the plume. The sudden drop at $\tau \sim 2.1$ corresponds to the shedding of smaller vortex pairs. Curves 12–15 represent the evolution of the levels near the boundary of the ascending plumes, and peaks in each curve represent break-offs of isolevel curves.

We now focus on how the penetration depth h grows in time, and how this temporal evolution depends on various control parameters in the simulations. Figure 23 shows curves of h versus τ for our two-dimensional simulations. We first note that at early time, the ascending h (figure 23*a*) does scale with τ^2 from $\tau^2 \sim 0.2$ to $\tau^2 \sim 3.0$. After $\tau^2 = 3.0$, the plumes have reached a terminal velocity and therefore travel at a constant speed, which is often observed in plumes without sustaining sources. We further note that the higher the Reynolds number, the faster the plume penetrates (cf. curve 1 and curve 2). We also observe faster penetration as we increase the diffusivity ratio (ν/κ) (cf. curve 2 and curve 3), which is a direct result of weaker stabilization for smaller diffusivity. We have also varied the initial perturbation amplitude (cf. curves 1 and 4, and curves 2 and 5): for perturbation of amplitude below 8% of the total box height, we find that the larger the initial perturbation, the faster the plume penetrate. The penetration depth depends linearly on the initial amplitude until $\tau \sim 1.4$, where nonlinearity may have set in to amplify the dependence on the initial state (cf. curve 2 and curve 5). We also note that the penetration of the heavy fluid into the light fluid remains more or less similar as we vary these parameters. The strong dependence of the ascending structure on the parameters is not reflected in the dynamics of the descending structures. This demonstrates that, with this form of initial perturbation, the ascending structures have different dynamics than the descending structures despite the low Atwood number adopted under the Boussinesq

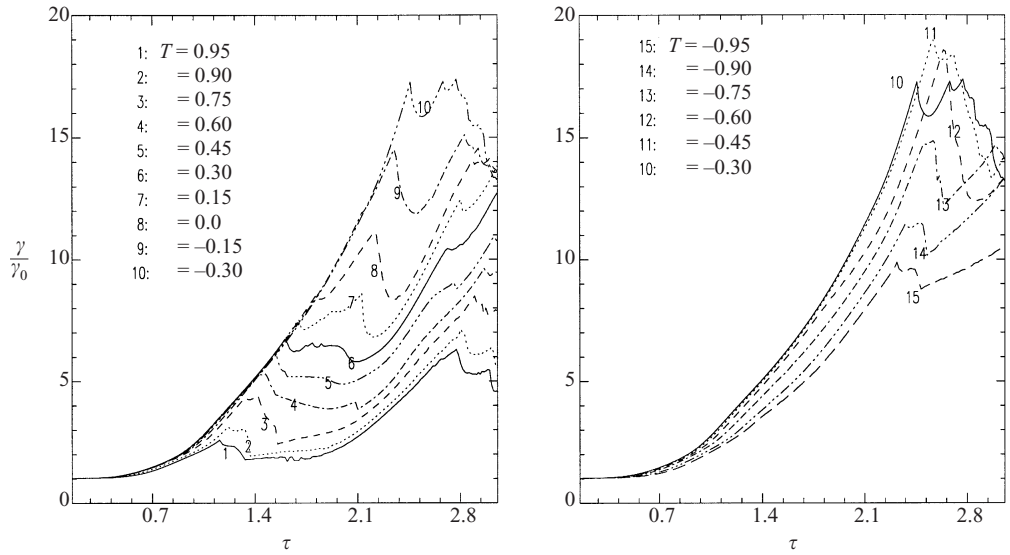

FIGURE 22. Amplification of arclength as a function of time for 15 different isolevels (two-dimensional).

approximation. This is certainly not the case if we perturb the interface with symmetric disturbances.

5.2. *Comparison between two-dimensional and three-dimensional plumes*

In this section we present results from simulations of both two-dimensional and three-dimensional single plumes for the first set of parameters in table 2. The differences between two and three-dimensional plumes are manifested in various aspects. In figure 24 we display the plume structures (at the same penetration depth) in both two and three dimensions. We also compute various quantities along the isothermal contours, and basically the same spatial structures are found in the three-dimensional plumes: the vorticity goes to zero at the cap head, the maximum circulation occurs around the neck, and positions of temperature gradient extrema are also points of vorticity extrema. The only discernible difference between two and three dimensions is the magnitude: the three-dimensional thermal gradient has a higher maximum at the cap head, and the advective heat transport (both vertical and horizontal components) in three dimensions is much smaller compared to the two-dimensional heat transport. This difference in the efficiency of heat transport explains the thinning of the two-dimensional stem as opposed to a constant width of the three-dimensional stem observed in our simulations. From our simulations, we also conclude that, for the same parameters, the cylindrically symmetric plumes (our three-dimensional plumes) travel much faster than the planar plumes (our two-dimensional plumes).

As seen in figure 25, the penetration depth in three dimensions increases faster with time than in the two-dimensional case, and eventually reaches almost 2 times the two-dimensional penetration depth at the end our our simulations. In order to understand this difference, we have calculated the temporal evolution of the ratio of total kinetic energy to the potential energy, and the partition of kinetic energy (which we break up into its two components, namely the total kinetic energy associated with vertical motions and with horizontal motions). Thus, in figure 26(*a*) we plot the energetic ratio versus τ, and show the evolution of the kinetic energy partition as a

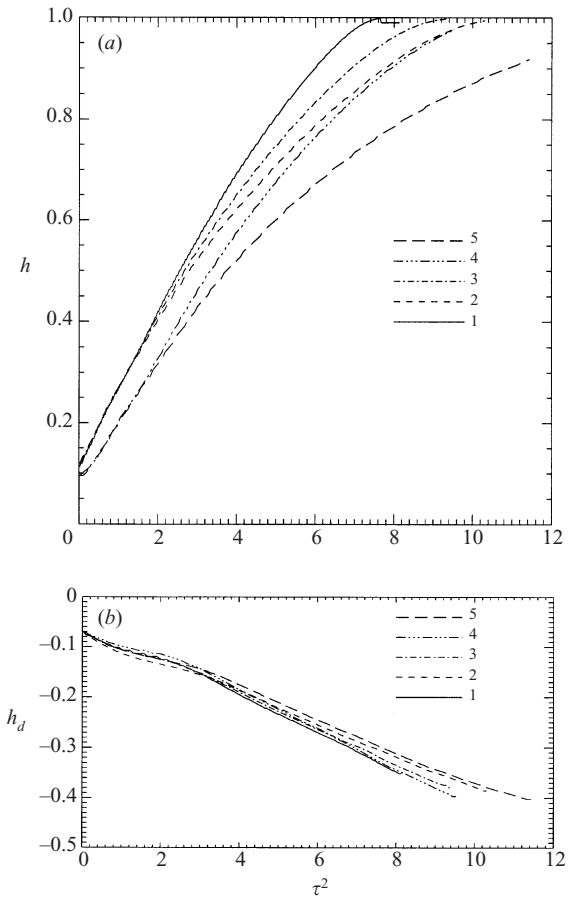

FIGURE 23. Penetration depth versus τ^2 for the two-dimensional single plumes: (*a*) the ascending boundary and (*b*) the descending boundary. The numbers are the run numbers listed in table 2.

function of time in figure 26(*b*). First, we point out that the rate of conversion of potential energy to kinetic energy is roughly the same in two and three dimensions. Secondly, we note that partitioning of the kinetic energy into horizontal and vertical components is different in two and three dimensions (with a larger fraction of the kinetic energy going to horizontal motions in the two-dimensional case). Based on these facts, we can now attribute the increased effectiveness of plume penetration in three dimensions to the fact that while more potential energy is released per unit time in two-dimensional than in three-dimensional, the partitioning of the resulting kinetic energy into its components drastically favours the directed vertical component in three dimensions, but not in two, into the vertical component of the flow kinetic energy, so that the three-dimensional plumes go faster and penetrate deeper in the same amount of time than their two-dimensional counterparts.

5.3. *Application of the single plume model and future direction*

We apply the plume model to our single plume simulations and find 'good' agreement as we fit the penetration depth h to the model (in the sense that the absolute error is less than 1% over the whole evolution). A typical example is shown in figure 21(*b*), where the dashed line is the least-square fit for the free-falling law, and the dash-

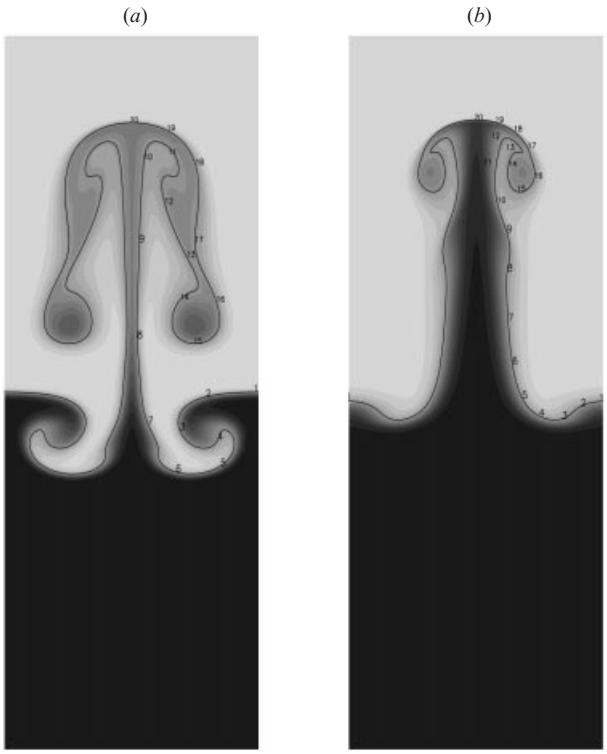

FIGURE 24. Comparison of (*a*) two-dimensional and (*b*) three-dimensional plume structures: geometric shape. The solid line is the $T = 0.7$ isothermal contour.

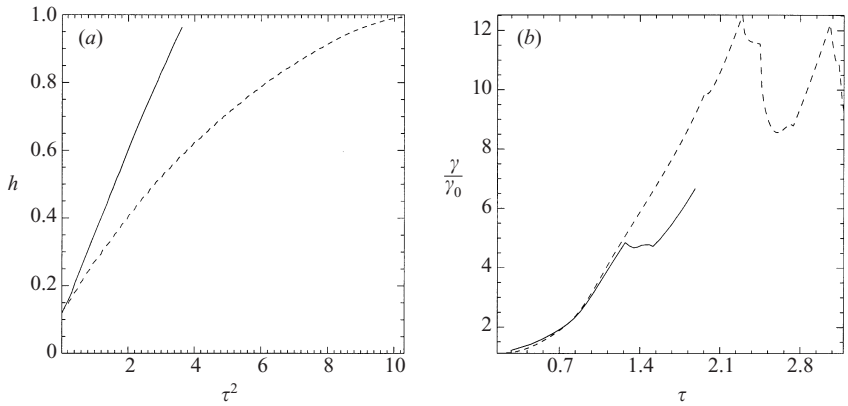

FIGURE 25. (*a*) Penetration depth and (*b*) the arclength of $T = 0$ isothermal curve: two-dimensional (dashed lines) versus three-dimensional (solid lines).

dotted line is the least-square fit for the plume model. We clearly see that the plume model captures the whole evolution, and the deviation is small compared to the τ^2 fit. When we apply the plume model to the random case (figure 27), the existence of three evolutionary phases prohibits a physically meaningful fit for the whole duration of the evolution, and a reasonably good fit is found for early evolution: $2.6 \leqslant \tau^2 \leqslant 13.4$,

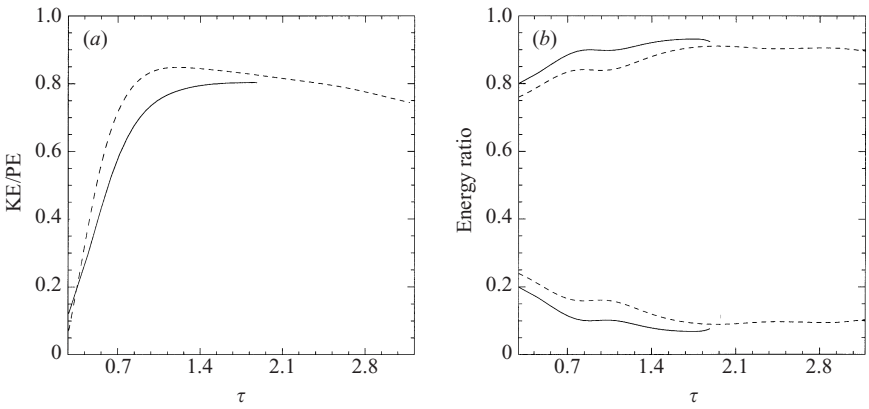

FIGURE 26. (*a*) Ratio of total kinetic energy to total potential energy available in the system as a function of τ. (*b*) Vertical partition of the total kinetic energy and horizontal partition of the kinetic energy as functions of τ. In both panels, we plot two-dimensional (dashed lines) together with three-dimensional simulations (solid lines).

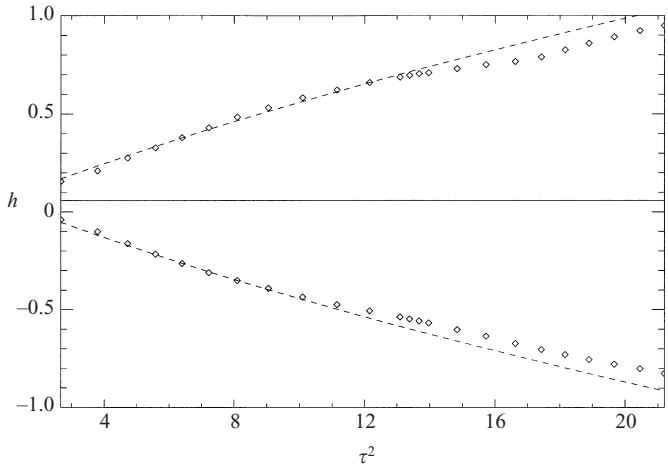

FIGURE 27. The three-dimensional random case revisited: the diamonds are from the simulations and the dashed lines are the fits of the analytic plume model to the data during the first free-falling phase.

where the effective acceleration from this fit is $\alpha \sim 0.03$. As shown in figure 27, the evolution deviates from the fit at $\tau^2 \sim 11$, just after the beginning of the mixing phase as discussed in § 3. This is an indication that the interaction of plumes with the background flow is substantial enough to arrest the free-falling propagation of the mixing zone. To incorporate this interaction with the background flow into the single plume model, one needs an equation for the energy evolution of the plume, and also an additional momentum term in equation (4.1) to describe the momentum transfer between the horizontal motion and the vertical motion. The interaction between plumes, such as merging, also makes an important contribution to the evolution of plumes as they expand in size and get closer to each other. This is a challenging future direction and is currently under investigation.

6. Summary and conclusions

We have performed numerical simulations in both two and three dimensions with relevant length scales arranged such that the thickness of the interface between the two fluids remains the same throughout the simulations. We have found dramatic differences between two-dimensional and three-dimensional flows with the aid of average quantities.

We first perturbed the RT interface with 'random' perturbations and investigate the evolution of the mixing zone in both two and three dimensions with the aid of averaged quantities. Scaling of the mixing zone width with τ^2 is found in both two and three dimensions, but only during selected intervals of time. Moreover, we find the three-dimensional mixing zone expands two times faster than the two-dimensional mixing zone. An important finding in this respect is that we can identify three phases of evolution for the three-dimensional mixing zone: the first is the free-falling phase just after the linear growth period (after 6 e-folding times, § 3), the second is the mixing phase where the free falling slows down and more mixing is generated as a result of enhanced horizontal motions, as illustrated in § 3; the third is another free-falling phase during which the broading of the mixing zone resumes the τ^2 scaling, when the big plumes near the edge become decoupled from the mixing zone and propagate on their own. Whether all of these phases are observed is likely to depend on the aspect ratio of the experimental domain. In the two-dimensional single plume case, we explore the parameters to demonstrate the effect of initial conditions on the broadening of the mixing zone and thus the effective acceleration α. Through energetic analysis, we are able to attribute the difference between two- and three-dimensional flows to the fact that in two dimensions, more energy goes into highly correlated horizontal and vertical motion (i.e., vortical motions) than into directed motions along the gravitational direction (three-dimensional).

We have discussed two analytic Rayleigh–Taylor models relevant to our computations (the bubble-competition model (Zufiria 1987) and the point-vortex model (Aref & Tryggvason 1989), which are effectively two extreme limits of the two-dimensional incompressible RT instability from the point-source point of view. The essential physical features found in both models are also key constituents of the buoyancy–drag plume model, in which each single plume experiences an acceleration due to the density contrast, and also a deceleration, which is due to a combination of viscous drag and the horizontal shear flows in the ambient background. We discuss how the plume model serves to connect the two models on physical grounds, and point out that the plume model actually contains more physical features, such as the coupling of the plumes with the mixing zone via the interaction between a background flow (inside the mixing zone) and flows in the stems of the plumes (whose heads are pushing the envelope of the mixing zone). Furthermore, we show that for the miscible vortex pair, both circulation (Γ) and penetration depth (h) scale with τ^2 for the same duration of time. This illustrates the close connection between the plumes and the point vortex pairs. In addition, we also strengthen the connection by comparing the evolution of the RT interface in the miscible case with that in the immiscible case. The extension of the single plume model to multi-plume systems is of great interest and is now under investigation.

The success of the buoyancy–drag model is an indication of the fundamental physical ingredients of the RT instability. Each bubble can be considered as an internal point source, and the curvature of the bubble evolves according to the internal source strength and the relative positions of the internal source and the bubble boundary. The internal point source is fed by the flow from below the bubble, namely the stem

connecting the cap head of the bubble. The coupling of the stem with the background flow, then, determines the strength of the internal source. All these features are ingredients of the plume model, which is, strictly speaking, an empirical model for plumes in both laminar and turbulent flows. Therefore, we find the buoyancy–drag plume model to give an adequate description of the various physical processes that we have observed. The extension of this single plume model to incorporate the coupling of plumes, merger events, and the background flow interaction is challenging and will no doubt bring us more insight into the RT instability.

This work was supported as part of the validation program of the Center for Astrophysical Thermonuclear Flashes, supported by the DOE/ASCI Alliances program at the University of Chicago. We would like to acknowledge extensive discussions of the Rayleigh–Taylor problem with N. J. Balmforth, J. Biello, A. Cook, G. Dimonte, B. Fryxell and L. Howard. The motivation and stimulation were provided by the 'alpha group' project, led by G. Dimonte.

REFERENCES

Alon, U., Hecht, J., Mukamel, D. & Shvarts, D. 1994 Scale invariant mixing rates of hydrodynamically unstable interfaces. *Phys. Rev. Lett.* **72**, 2867–2870.

Alon, U., Shvarts, D. & Mukamel, D. 1993 Scale-invariant regime in Rayleigh–Taylor bubble-front dynamics. *Phys. Rev.* E **48**, 1008–1014.

Aref, H. & Tryggvason, G. 1989 Model of Rayleigh–Taylor instability. *Phys. Rev. Lett.* **62**, 749–752.

Chandrasekhar, S. 1961 *Hydrodynamic and Hydromagnetic Stability*. Clarendon

Cook, A. W. & Dimotakis, P. 2001 Transition stages of Rayleigh–Taylor instability between miscible fluids. *J. Fluid Mech.* **443**, 69–99.

Dahlburg, J. P. & Gardner, J. H. 1990 Ablative Rayleigh–Taylor instability in three dimensions. *Phys. Rev.* A **41**, 5695–5698.

Dimonte, G. & Schneider, M. 1999 Density ratio dependence of Rayleigh–Taylor mixing for sustained and impulsive acceleration histories. *Tech Rep.*

Dubey, A. & Clune, T. 1999 Optimization of a parallel pseudospectral MHD code. *Proc. of Frontiers, the Seventh Symp. on the Frontiers of Massively Parallel Computation, 1999.*

Duff, R. E., Harlow, F. H. & Hirt, C. W. 1962 Effects of diffusion on interface instability between gases. *Phys. Fluids* **5**, 417–425.

Fermi, E. 1951 Taylor instability of an incompressible liquid. *The Collected Papers of Enrico Fermi* (ed. E. Segre), vol. 2, pp. 816, 821.

He, X., Zhang, R., Chen, S. & Doolen, G. D. 1999 On three-dimensional Rayleigh–Taylor instability. *Phys. Fluids* **11**, 1143–1152.

Hill, F. M. 1975 A numerical study of the descent of a vortex pair in a stably stratified atmosphere. *J. Fluid Mech.* **71**, 1–13.

Kane, J. & Arnett, D. 1998 Scaling supernova hydrodynamics to the laboratory. *The Conf. Proc. of the APS DPP98 meeting, Nov. 1998.*

Li, X. L. 1993 Study of three-dimensional Rayleigh–Taylor instability in compressible fluids through level set method and parallel computation. *Phys. Fluids* A **5**, 1904–1913.

Lighthill, M. J. 1986 *An Informal Introduction to Theoretical Fluid Mechanics*. Oxford University Press.

Linden, P. F., Redondo, J. M. & Youngs, D. L. 1994 Molecular mixing in Rayleigh–Taylor instability. *J. Fluid Mech.* **265**, 97–124.

Moses, L., Zocchi, G. & Libchaber, A. 1993 An experimental study of laminar plumes. *J. Fluid Mech.* **251**, 581–601.

Read, K. I. 1984 Experimental investigation of turbulent mixing by Rayleigh–Taylor instability. *Physica* **12 D**, 45–58.

Sakagami, H. & Nishihara, K. 1990 Three-dimensional Rayleigh–Taylor instability of spherical systems. *Phys. Rev. Lett.* **65**, 432–435.

Schneider, M. B., Dimonte, G. & Remington, B. 1998 Large and small structure in Rayleigh–Taylor mixing. *Phys. Rev. Lett.* **80**, 3507–3510.

Sharp, D. H. 1984 An overview of Rayleigh–Taylor instability. *Physica* **12 D**, 3–18.

Town, R. J. P. & Bell, A. R. 1991 Three-dimensional simulations of the implosion of inertial confinement fusion targets. *Phys. Rev. Lett.* **67**, 1863–1866.

Tryggvason, G. 1988 Numerical simulations of the Rayleigh–Taylor instability. *J. Comput. Phys.* **75**, 253–282.

Tryggvason, G. & Unverdi, O. 1990 Computations of three-dimensional Rayleigh–Taylor instability. *Phys. Fluids* A **2**, 656–659.

Tufo, H. & Fischer, P. F. 2001 Fast parallel direct solvers for coarse grid problems. *J. Parallel Distr. Comput.* **61**, 151–177.

Turner, J. S. 1973 *Buoyancy Effects in Fluids*. Cambridge University Press.

Werne, J. 1994 Plume model for the boundary-layer dynamics in hard turbulence. *Phys. Rev.* E **49**, 4072.

Werne, J. 1995 Incompressibility and no-slip boundaries in the Chebyshev–Tau approximation – correction to Kleiser and Schumann influence matrix-solution. *J. Comput. Phys.* **120**, 260–265.

Yabe, T., Hoshino, H. & Tsuchiya, T. 1991 Two and three dimensional behavior of Rayleigh–Taylor and Kelvin-Helmholtz instabilities. *Phys. Rev.* A **44**, 2756.

Youngs, D. 1984 Numerical simulation of turbulent mixing by Rayleigh–Taylor instability. *Physica* **12 D**, 32–44.

Youngs, D. 1991 Three-dimensional numerical simulation of turbulent mixing by Rayleigh–Taylor instability. *Phys. Fluids* A **3**, 1312–1320.

Zufiria, J. 1987 Bubble competition in Rayleigh–Taylor instability. *Phys. Fluids* **31**, 440–446.